Characterization of silicon microstrip sensors for space astronomy

Jia-Ju Wei[1,2] · Jian-Hua Guo[1,2] · Yi-Ming Hu[1,2]

Abstract Silicon microstrip detectors are widely used in experiments for space astronomy. Before the detector is assembled, extensive characterization of the silicon microstrip sensors is indispensable and challenging. This work electrically evaluates a series of sensor parameters, including the depletion voltage, bias resistance, metal strip resistance, total leakage current, strip leakage current, coupling capacitance, and interstrip capacitance. Two methods are used to accurately measure the strip leakage current, and the test results match each other well. In measuring the coupling capacitance, we extract the correct value based on a SPICE model and two-port network analysis. In addition, the expression of the measured bias resistance is deduced based on the SPICE model.

Keywords Silicon microstrip sensor · Space astronomy · Characterization · SPICE model

✉ Jia-Ju Wei
  weijj@pmo.ac.cn

1 Purple Mountain Observatory, Chinese Academy of Sciences, Nanjing 210023, China

2 Key Laboratory of Dark Matter and Space Astronomy, Chinese Academy of Sciences, Nanjing 210023, China

1 Introduction

Γ-ray detection is one of the most important observation methods in space astronomy. Recent studies showed that the high-energy γ-ray's spectrum and distribution can be used to explore the physical characteristics and distribution of the dark matter. By contrast, X-ray detection is also important in space astronomy. For example, hard X-ray solar observation can probe nonthermal electrons accelerated in the solar atmosphere. To accurately detect the γ-ray and X-ray distributions, a tracker with a very high spatial resolution is needed. Although there are many candidates [1–4], the silicon microstrip detector [5–8] is one of the most suitable candidates because it has excellent spatial resolution (lower than 1.8 μm was mentioned in reference [9]). In addition, silicon microstrip detectors can extend the detection area by forming a cascade structure (i.e., the so-called ladder [10]) without adding extra readout electronics. This feature is very important for high-energy space astronomy detection, which needs a large detecting area but low power consumption.

Silicon microstrip detectors are widely used in experiments for space astronomy, e.g., Payload for Antimatter Exploration and Light-nuclei Astrophysics (PAMELA) [11, 12], Light Imager for γ-ray Astrophysics (AGILE) [13, 14], γ-ray Large Area Space Telescope (Fermi-GLAST) [15, 16], Alpha Magnetic Spectrometer (AMS-02) [17, 18], Dark Matter Particle Explorer (DAMPE) [19, 20], and Focusing Optics X-ray Solar Imager (FOXSI) [21, 22]. Based on DAMPE's experience, our collaborative group proposes a new generation of space telescope, i.e., Very Large Area gamma-ray Space Telescope (VLAST). In the preliminary design, 18 tracking planes, each consisting of two layers of single-sided silicon

microstrip sensors, will be configured to measure the two orthogonal views perpendicular to the pointing direction of the detector.

Extensive characterization of the silicon microstrip sensors before assembling the detector is indispensable. Owing to the cascade structure, one bad sensor will deactivate the detecting "ladder" consisting of several sensors and generate a large "dead" area. On the other hand, the characterization process is challenging. Due to the on-chip parasitics, the silicon microstrip sensor acts as a complicated SPICE RC network [23, 24], so it is challenging to measure or extract the right parameters. In addition, the actual values of some parameters cause difficulties in the measurement, e.g., very low current, resistance, or capacitance. This work evaluates the main sensor parameters, including the depletion voltage, bias resistance, metal strip resistance, total leakage current, strip leakage current, coupling capacitance, and interstrip capacitance.

2 Basic sensor structure

In this work, we study a single-sided AC-coupled sensor (shown in Fig. 1) using a silicon wafer of 320 μm in thickness from Hamamatsu Photonics. The electrical resistivity of the N-doped silicon wafer is on the order of several $k\Omega \cdot cm$, and the chip size is 95 mm × 95 mm. The P^+ implant strips are 48 μm wide and 93 mm long, with a pitch of 121 μm. Each implant strip is biased with a poly-silicon resistor that is connected to a bias ring. The AC coupling is obtained using a silicon oxide layer between the implant strip and the floating metal strip. To prevent microdischarge at the edges, the metal strip covers the implant strip edges with a 4-μm overhang [25]. In addition, the AC pads and DC pads of the sensor allow testing access to the metal strip and the implant strip, respectively.
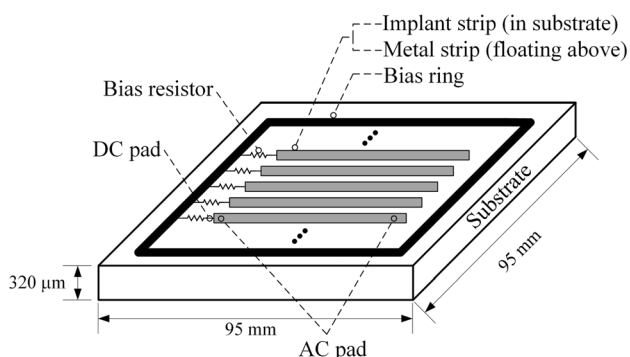
3 Characterization of sensor

Because silicon microstrip sensors are very fragile and sensitive to contamination during transport, storage, and picking, we must evaluate them extensively before assembling them onto the hybrid board. By contrast, some sensor parameters may deviate from the nominal value by a range, so accurate measurements are needed to determine the actual value. In addition, the characterization process can improve our understanding of the sensor's working mechanism.

3.1 Depletion voltage

A silicon microstrip sensor consists of hundreds of strips, and each P^+ implant strip together with the N-doped substrate forms a typical PN junction approximately. When a reverse bias voltage is applied to the sensor, a depletion layer free of mobile carriers appears. The depletion voltage is the bias voltage, which extends the depletion layer to the thickness of the sensor.

According to Hamamatsu Photonics, the wafer resistivity of the silicon microstrip sensor is in the range of 5–10 $k\Omega \cdot cm$. We can roughly estimate the depletion voltage [26] by

$$V_{depl} = \frac{L^2}{2\rho\epsilon\epsilon_0\mu_e},\tag{1}$$

where L is the wafer thickness, μ_e is the electron mobility, ρ is the wafer resistivity, ϵ is the vacuum dielectric constant, and ϵ_0 is the silicon relative dielectric constant. The calculated depletion voltage is in the range of 34–67 V, approximately.

To obtain the actual depletion voltage, we measured the bulk capacitance of the sensor by sweeping the bias voltage. Figure 2 shows the measurement setup. This test configuration uses a Keysight E4980A LCR meter to measure capacitances. The open and short corrections of the E4980A are implemented to compensate for any stray
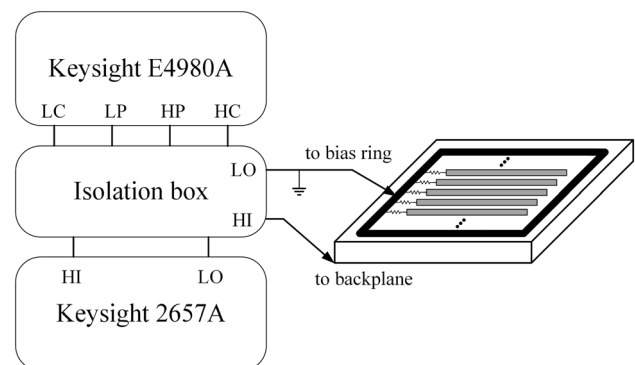

Fig. 1 Structure of silicon microstrip sensor

Fig. 2 Configuration for depletion voltage measurement

admittances and residual impedances, respectively. To make the sensor work properly, a bias voltage should be applied. Although the Keysight E4980A has a built-in DC bias of up to 40 V, we still need an independent source meter that can provide a DC voltage exceeding the estimated depletion voltage (i.e., 67 V). A Keithley 2657A source meter is chosen. An isolation box (i.e., Keysight 16065A) is used to mix the DC bias (from the source meter) and the AC test signal (from the LCR) together, and then the outputs are connected to the sensor, which is located in the shielding chamber of a probe station.

As the reverse bias voltage increases, the bulk capacitance per unit area C_{bulk} decreases to a constant when the maximum depletion depth is achieved. We rearrange Eq. (3) in [27] as

$$\frac{1}{C_{bulk}^2} = \begin{cases} \dfrac{2V_{bias}}{q\epsilon_{si}|N_{effect}|} & V_{bias} \leq V_{depl} \\[2ex] \dfrac{d_{depl}^2}{\epsilon_{si}^2} & V_{bias} > V_{depl} \end{cases}, \quad (2)$$

where d_{depl} is the full depletion depth, q is the electrical charge, $N_{effective}$ is the effective charge carrier density, and ϵ_{si} is the dielectric constant of the bulk silicon.

A plot of $1/C_{bulk}^2$ versus V_{bias} based on the measured data is shown in Fig. 3. We fit the slope and flat parts of the data points with a straight line. The depletion voltage can be extracted at the intersection point of these fitting lines, i.e., 36.5 V. To reduce the charge collection time and the ballistic deficit [28], we often bias the sensor at a higher voltage (80 V), i.e., twice the depletion voltage.
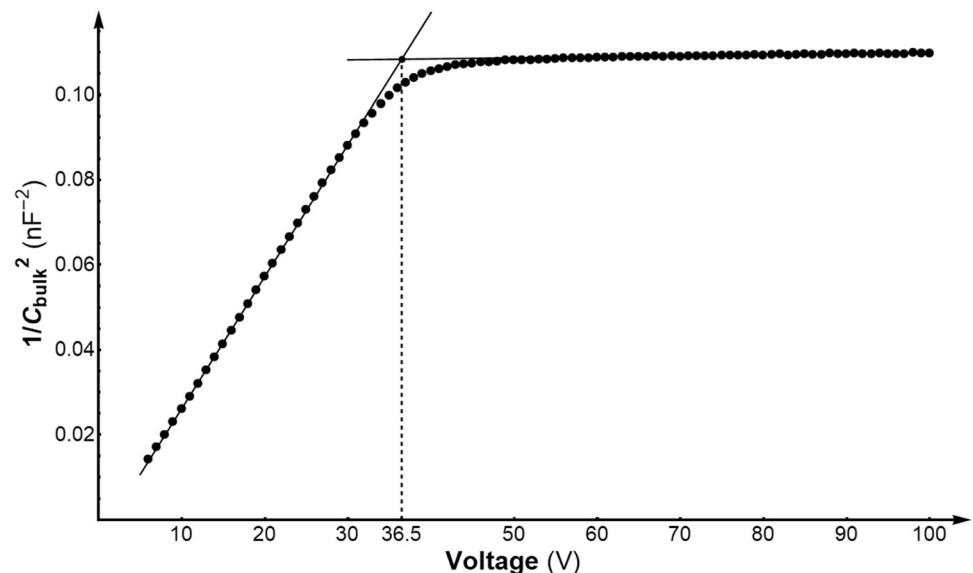
3.2 Bias resistance

The bias resistor's functions are to bias each strip at a specific potential and to isolate different strips. The sensor uses a doped poly-silicon meandering line, i.e., poly-silicon resistor, to connect the strip's endpoint and the bias ring. It is incorrect to measure the bias resistance by just applying a voltage source and measuring the current at the terminals (i.e., the DC pad and the bias ring). In this incorrect circumstance, the main part of the testing current is bypassed through the DC pad (connected to the source and meter terminal), the corresponding strip, the backplane, other strips, and then to the bias ring (connected to the common ground terminal). Thus, the measured resistance is much lower than the actual value. This conclusion was confirmed by measurements.

The correct configuration to measure the bias resistance is shown in Fig. 4. A multimodule integrated parameter analyzer, the Keithley 4200A-SCS, is adopted. We select three types of modules in the parameter analyzer: source measure unit (SMU), ground unit (GNDU), and preamplifier (PA). Next, we set up a local sense configuration [29]. The SMU module is very flexible and can be configured by software as the source or the meter. In this configuration, the second SMU provides a bias voltage that depletes the substrate to block the bypass. The first SMU applies a small testing voltage and measures its current at the same time, so the resistance can be calculated by the measured voltages and currents.

Due to the on-chip parasitics, the silicon microstrip sensor can be modeled by a complicated SPICE RC network [23]. The SPICE model at DC frequency, shown in Fig. 5, is used to accurately analyze the calculated resistance. In this model, R_{poly} represents the poly-silicon

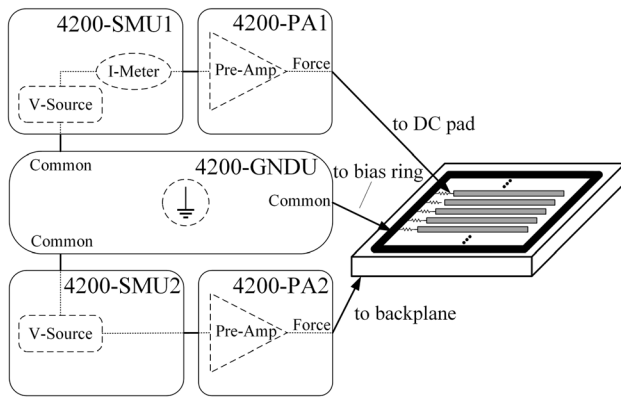**Fig. 3** Depletion voltage extraction

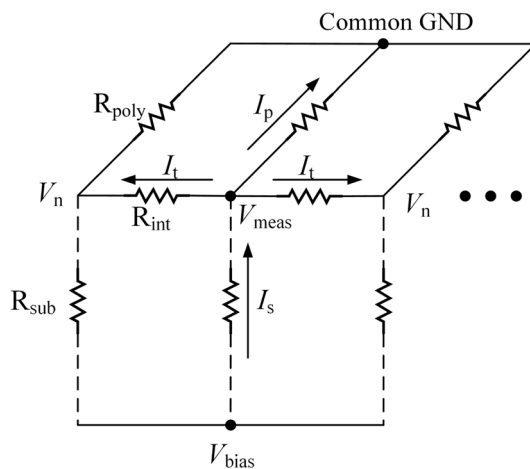Fig. 4 Configuration for bias resistance measurement

Fig. 5 SPICE model of bias resistance measurement

resistance, R_{int} represents the interstrip resistance, and R_{sub} represents the strip's backplane resistance. In addition, node potentials and path currents are marked in the figure. The unmarked current I_{meas} is at node V_{meas}, and its direction points into the paper. We can easily get the relation as

$$I_{meas} + \frac{V_{bias} - V_{meas}}{R_{sub}} = \frac{V_{meas}}{R_{poly}} + 2 \times \frac{V_{meas} - V_n}{R_{int}}.$$

(3)

The measured resistance is defined as the ratio of the voltage change and the current change:

$$R_{meas} = \triangle V_{meas} / \triangle I_{meas} = R_{poly} || R_{sub} || (0.5 R_{int}).$$

(4)

Because R_{sub} and R_{int} are on the order of gigaohms while R_{poly} is on the order of megaohms, the measured resistance is approximately equal to the poly-silicon resistance. As shown in Fig. 6, the measured $V - I$ curve can be well fitted by a straight line, and the slope of the fitting line is 43

MΩ, which represents the bias resistance. The measured bias resistance seems reasonable because it lies in the middle of the range of 20–60 MΩ from the manufacturer's specifications.

3.3 Metal strip resistance

The metal strip floats above the silicon oxide layer, couples the charge signal generated in the underlying depletion area, and transmits the signal to the external preamplifier in the readout ASICs. Due to its tiny width and thinness, the resistance of the long metal strip cannot be sufficiently low, and thus it contributes a thermal noise in series with the preamplifier's input. According to Fig. 4 in [10], as the length of the ladder increases, the equivalent noise charge (ENC) owing to the metal strip resistance gradually becomes the dominant noise, so it is necessary to accurately measure the resistance.

Because the metal strip resistance is relatively low (about tens of ohms), a full-Kelvin remote sensor measurement [29] should be adopted to eliminate the cable resistance and the probe-to-pad resistance. The measurement configuration is shown in Fig. 7. Using a set of testing cables, current is forced through the left AC pad, the metal strip, and then the right AC pad. At the same time, the voltage across the metal strip is measured using a set of sensing cables. The two sets of cables are only allowed to be connected to the corresponding AC pad by the probe tips. The testing current sweeps from 1 to 100 mA in steps of 1 mA, so 100 resistance samples are obtained by calculating the ratio of the measured voltage and the corresponding current. We randomly select three metal strips (No. 100, No. 103, and No. 105), and the measured resistances are 30.292 ± 0.018 Ω, 30.300 ± 0.018 Ω, and 30.305 ± 0.007 Ω, respectively.

3.4 Total leakage current

According to the sensor's structure and working mechanism, the signal is inherently added to the leakage current, so the leakage fluctuation will inevitably affect the sensor's signal-to-noise ratio (S/N) and energy resolution. Thus, the leakage current is one of the main noise resources in the sensor and is often taken as a primary measure of the sensor's quality.

The sensor's total leakage current is equal to the sum of all strips and can represent the average leakage level. We can measure the total leakage current by the configuration shown in Fig. 8. In order to protect the sensor against damage, we activate a dual sweeping bias voltage from 1 to 100 V and then from 100 to 1 V, with a step of 1 V. In addition, triaxial cables are used to connect the parameter analyzer and the sensor to guarantee measurement
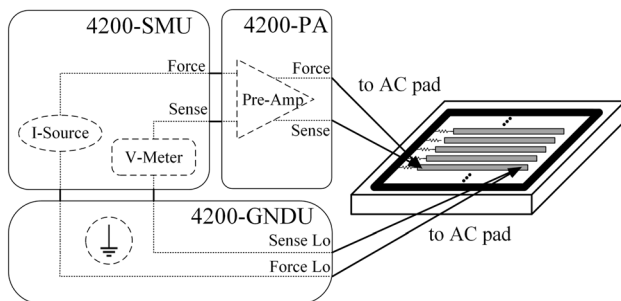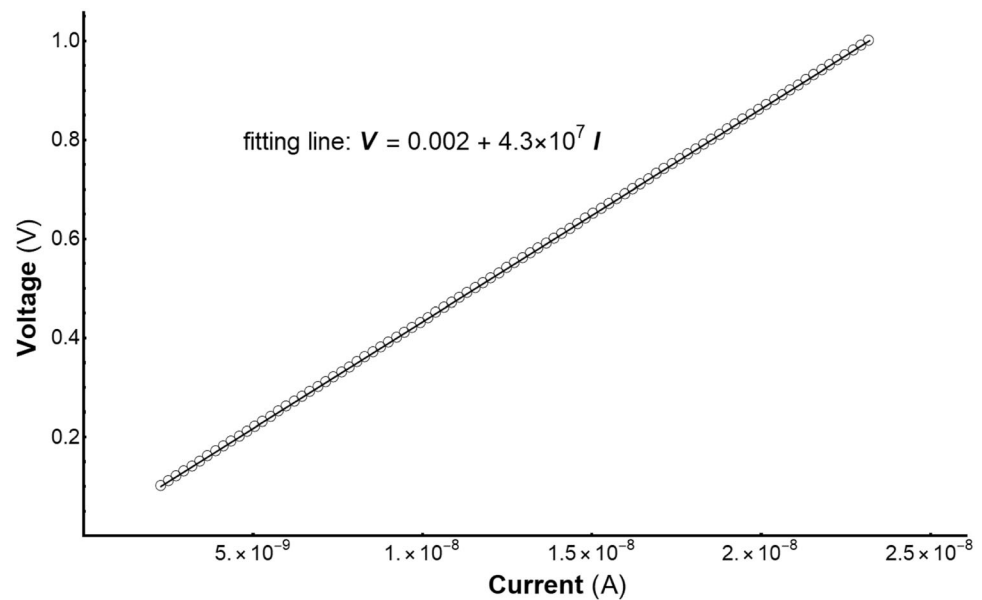
Fig. 6 Measurement result of bias resistance

fitting line: $V = 0.002 + 4.3 \times 10^7 I$

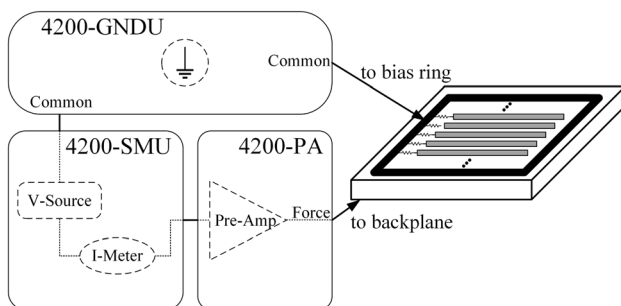**Fig. 7** Configuration for metal strip resistance measurement

Fig. 8 Configuration for total leakage current measurement

accuracy. In addition, the leakage current is sensitive to environmental conditions, so we control the clean room's temperature and humidity at $20 \pm 1°C$ and $40 \pm 5\%$, respectively.

The measured $I - V$ characteristics of the total leakage current are shown in Fig. 9. As the reverse bias voltage increases, the total leakage current increases accordingly and gradually reaches saturation. It can be observed that the sensor's total leakage current is very low. The average
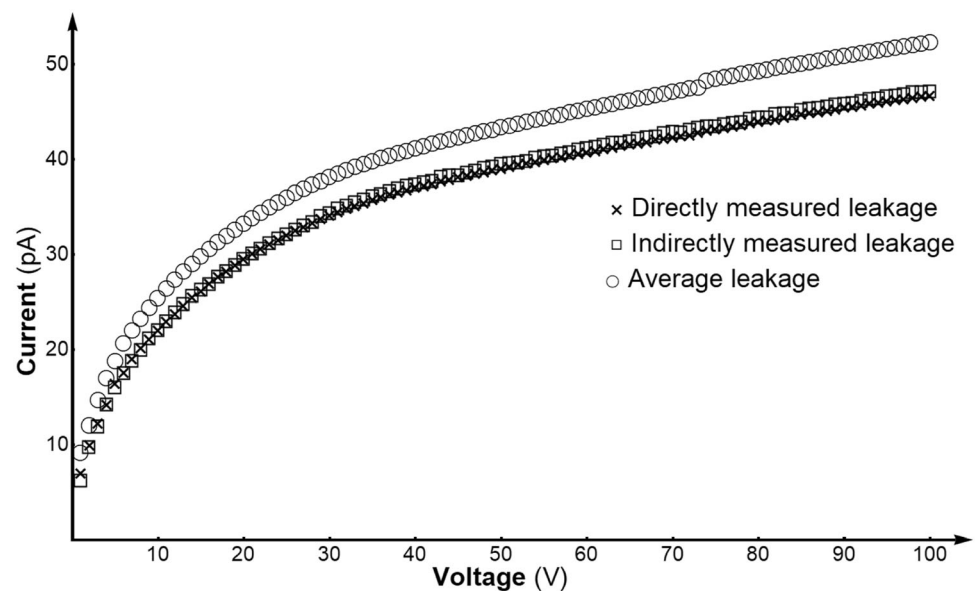
current density is on the order of 0.3 nA/cm^2 and 0.4 nA/cm^2 at the depletion voltage and operating voltage, respectively.

3.5 Strip leakage current

Due to fabrication defects and manipulation damage, a few implant strips may appear to have a much higher leakage current than the average leakage level. The value of the strip leakage current is used to identify these bad strips from hundreds of good ones. To accurately measure the strip leakage current, there are two challenges. First, each implant strip of our sensor is physically connected to the bias ring through a poly-silicon resistor, so the leakage currents of all strips converge to the bias ring, which is connected to the common ground. Thus, the device-under-test (DUT) strip's leakage current should be separated from the total leakage current. Second, because the strip leakage current is on the order of tens to hundreds of picoamperes, it requires a much lower system noise in the measurement.

Two measurement configurations are proposed in Fig. 10. To directly measure the strip leakage current, we configure the 1st SMU as a current meter (i.e., select I-Meter in this figure). In this configuration, the DUT strip's leakage current flows into the current meter, while the remaining strips' leakage currents flow into the common ground. These two parts of the total leakage current are separated by the DUT strip's poly-silicon resistor that is about tens of megaohms. The directly measured I–V curve is shown in Fig. 11, and it is similar to the total leakage current in Fig. 9 but much smaller.

We can also measure the strip's leakage current indirectly when the first SMU is configured as a voltage meter

Fig. 9 Measurement result of total leakage current
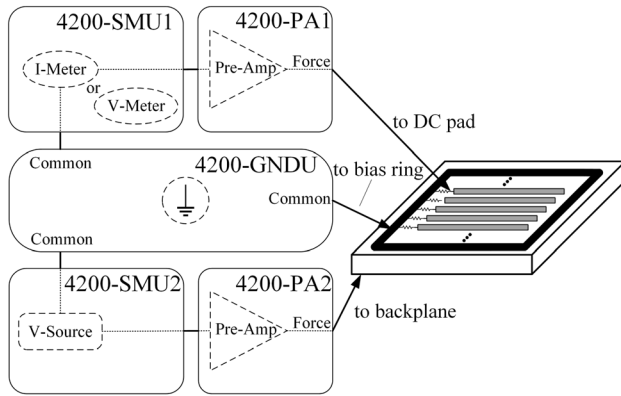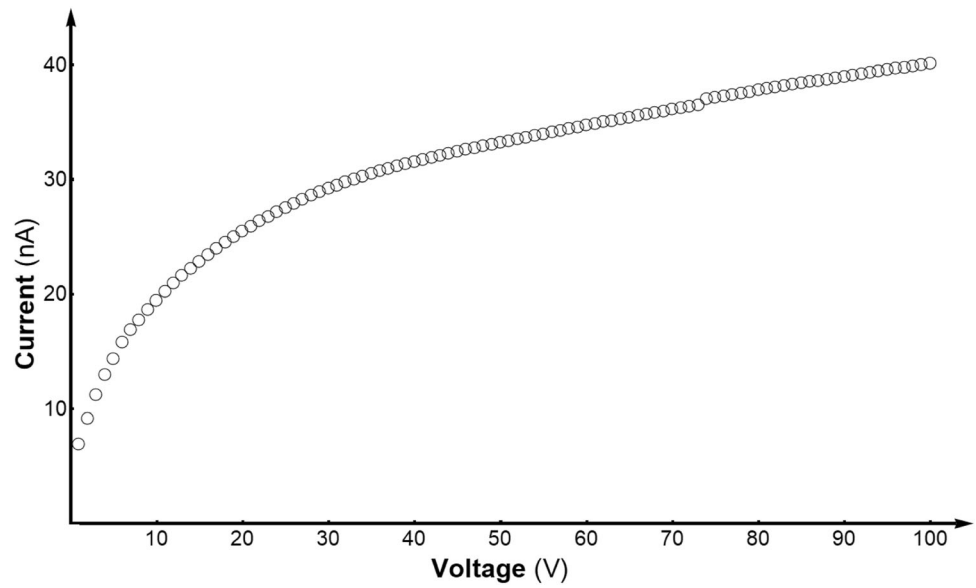
Fig. 10 Configuration for strip leakage current measurement

(i.e., select V-Meter in Fig. 10). In this configuration, the poly-silicon resistor and the strip's substrate resistor form a simple voltage divider, i.e.,

$$V_{measure} = V_{sweep} \times \frac{R_{poly}}{R_{poly} + R_{sub}}, \tag{5}$$

where $V_{measure}$ is the voltage measured by the voltage meter, and V_{sweep} is the sweep voltage applied by the voltage source.

In subsection 3.2, there is a small voltage drop between the DUT strip and its neighboring strips, so Eq. (4) includes the interstrip resistance. The indirect configuration here is similar to the configuration for the bias resistance

Fig. 11 Measurement result of strip leakage current

× Directly measured leakage
□ Indirectly measured leakage
○ Average leakage

measurement but without a testing signal injected into the DC pad. Because there is no such voltage drop, the input resistance when looking into the DC pad with respect to the common ground is

$$R_{\text{dc}} = R_{\text{poly}} || R_{\text{sub}}. \tag{6}$$

Because the interstrip resistance is very large compared with $R_{\text{poly}} || R_{\text{sub}}$, it is reasonable to assume that R_{dc} is equal to the measured bias resistance.

With Eqs. (5) and (6), we can get

$$R_{\text{poly}} = \frac{R_{\text{dc}} V_{\text{sweep}}}{V_{\text{sweep}} - V_{\text{poly}}} \ , \ R_{\text{sub}} = \frac{R_{\text{dc}} V_{\text{sweep}}}{V_{\text{poly}}}. \tag{7}$$

With Eq. (7), the strip leakage current is defined and calculated by

$$I_{\text{strip}} = \frac{V_{\text{sweep}}}{R_{\text{poly}} + R_{\text{sub}}} = \frac{V_{\text{poly}}(1 - V_{\text{poly}}/V_{\text{sweep}})}{R_{\text{dc}}}. \tag{8}$$

The indirectly measured result is shown in Fig. 11, and the average leakage current calculated from the total leakage current is also added. As shown in this figure, the directly and indirectly measured strip leakage currents match each other well, and both currents are close to the average leakage level.

3.6 Coupling capacitance

The coupling capacitor in the silicon microstrip sensor has two main functions. First, it couples the charge in the implant strip to the metal strip that is connected to the readout ASICs. Second, the coupling capacitor can isolate the readout ASICs from the sensor's bias voltage and leakage current. In our sensor, the coupling capacitor is implemented as a "metal–insulator–semiconductor" structure, and two terminals of the capacitor are the DC pad and AC pad of the DUT strip. Fig. 12 shows the measurement configuration. The high ports (HP and HC) and low ports (LP and LC) of the Keysight E4980A LCR meter are connected to the coupling capacitor's two terminals, while a Keithley 2657A provides a working bias voltage. The open and short corrections of the E4980A are implemented to guarantee the measurement accuracy.

The measured $C - f$ curve is shown in Fig. 13. In the figure, the curve indicates a strong dependence on the frequency. When the frequency is lower than 500 Hz, the measured capacitance is high and relatively stable. As the frequency increases, the capacitance drops dramatically. When the frequency is higher than 2 MHz, which is beyond our testing scope, the capacitance seems to approach zero.
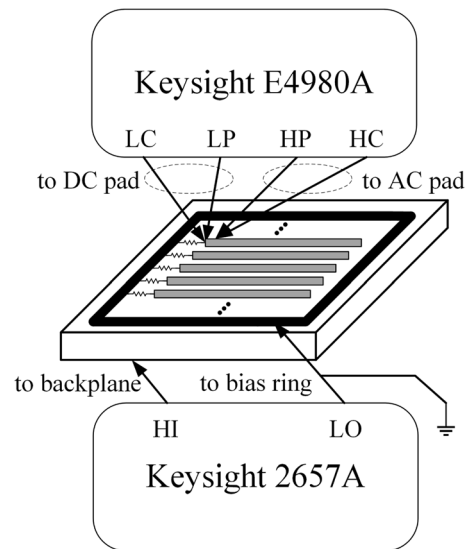

Fig. 12 Configuration for coupling capacitance measurement

To quantitatively analyze the measured $C - f$ curve, we divide the DUT strip's SPICE model into N unit cells, as shown in Fig. 14. Each unit cell comprises three components: R_{metal}/N and R_{implant}/N represent the unit cell's metal strip resistance and implant strip resistance, respectively, and C_{couple}/N is the unit cell's coupling capacitance. When the unit cell is treated as a two-port network, we can easily obtain its transmission matrix as

$$T_{\text{cell}} = \begin{pmatrix} 1 + \dfrac{j\omega C_{\text{couple}}(R_{\text{metal}} + R_{\text{implant}})}{N^2} & \dfrac{R_{\text{metal}} + R_{\text{implant}}}{N} \\ \dfrac{j\omega C_{\text{couple}}}{N} & 1 \end{pmatrix}. \tag{9}$$

Because the DUT strip's SPICE model is a cascade connection of N unit cells, the transmission matrix of the DUT strip equals the product of all cells' transmission matrices:

$$T_{\text{strip}} = T_{\text{cell}}^N = \begin{pmatrix} T_1 & T_2 \\ T_3 & T_4 \end{pmatrix}. \tag{10}$$

The capacitor looking into the DUT strip can be calculated as

$$C_{\text{meas}} = \frac{T_3}{j\omega T_1} \tag{11}$$

Although the analytical expression is complicated, we can give the limit value when the frequency is zero and infinity as

$$\lim_{\omega \to 0} C_{\text{meas}} = C_{\text{couple}} \ , \ \lim_{\omega \to \infty} C_{\text{meas}} = 0. \tag{12}$$

The limit values well match the shape of the $C - f$ curve in Fig. 13 and demonstrate that the coupling capacitance of

Fig. 13 Measurement result of coupling capacitance
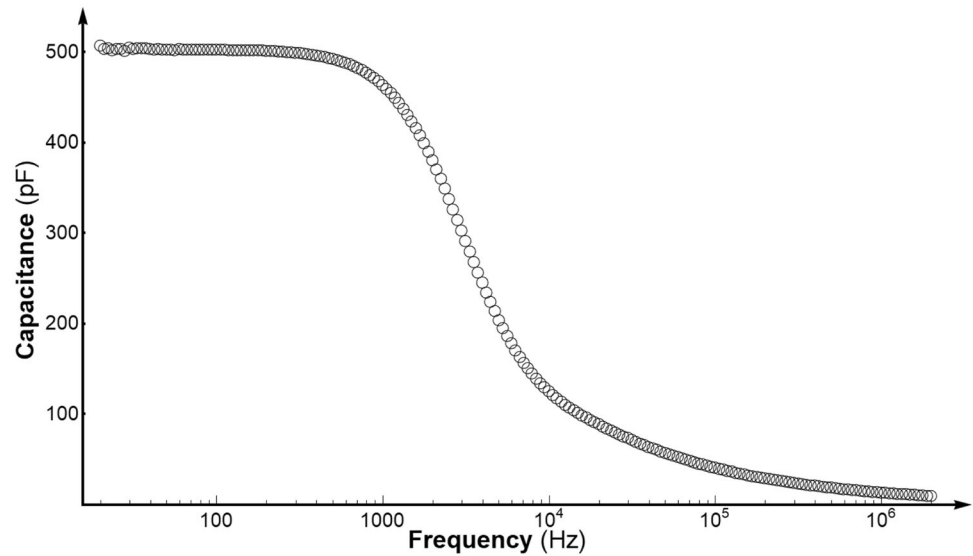
Fig. 14 SPICE model of coupling capacitance measurement
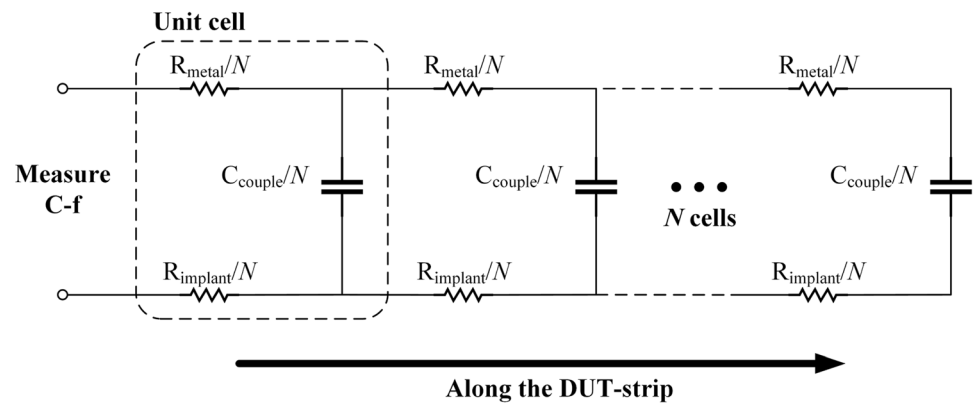
the DUT strip can be extracted from the measured curve at low frequencies. In our experiment, the extracted coupling capacitance of the DUT strip is 508 pF.

3.7 Interstrip capacitance

The interstrip capacitance is the main part of the total capacitance seen by the preamplifier input. According the product information of a typical readout ASIC [30], ENC induced by the ASIC is in proportion to the input capacitance, so the interstrip capacitance should be reduced to suppress noise. On the other hand, the interstrip capacitance should be increased to avoid a charge loss in the process of charge division. By measuring the interstrip capacitance, we can evaluate the noise induced by ASIC and the charge collection efficiency.

The measurement configuration is shown in Fig. 15. The high ports (HP and HC) of the Keysight E4980A LCR meter are connecting to the DUT strip's AC pad, and the low ports (LP and LC) are connected to its neighboring strip's AC pad. The open and short corrections are used. To
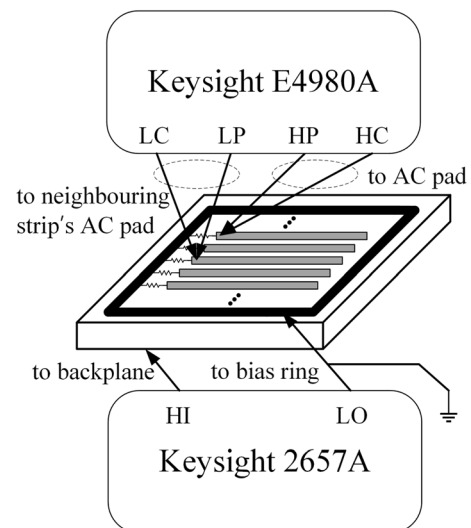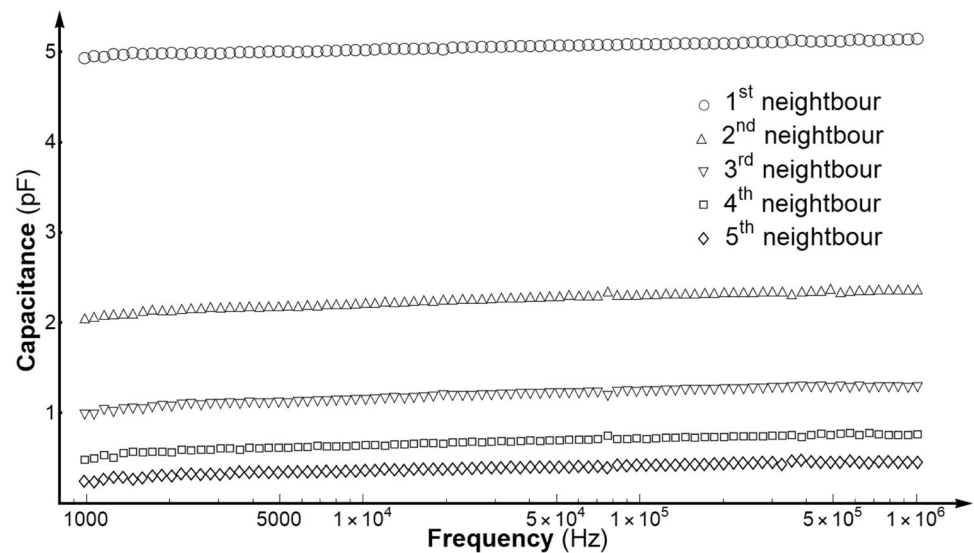

Fig. 15 Configuration for interstrip capacitance measurement

Fig. 16 Measurement result of interstrip capacitance

guarantee the sensor is in working condition, a bias voltage is applied by a Keithley 2657A.

Because the interstrip capacitance is very low (only a few picofarads), the impedance at low frequencies is very high. Thus, it is difficult to accurately measure the interstrip capacitance at low frequencies. Actually, the measured C–f curve fluctuates dramatically at low frequencies. To show the measured data clearly, we draw the C–f curve from 1 kHz in Fig. 16. As shown in the figure, we find that the interstrip capacitance is independent of the frequency and drops as the neighboring strip is farther away from the DUT strip. In our experiment, the extracted interstrip capacitances between the DUT strip and its neighbors are 5.15 pF, 2.38 pF, 1.29 pF, 0.75 pF, and 0.44 pF.

4 Conclusion

A silicon microstrip sensor used in space astronomy was extensively characterized in this work. To determine the depletion voltage, we measured the bulk capacitance and then fitted the measured data to extract the depletion voltage. In measuring the bias resistance, we first pointed out the necessity to apply a bias voltage in the test configuration. Second, a SPICE model was proposed to analyze the complex parasitics and deduce the expression of the measured result. Third, we linearly fitted the measured data and extracted the bias resistance according to the deduced expression. To accurately measure the metal strip resistance, we set up a full-Kelvin remote sensing configuration because the resistance was relatively low. The total leakage current was measured to evaluate the sensor's average leakage level. Direct and indirect measurement methods were adopted to characterize the strip leakage current, and the measured results matched each other well. In measuring the coupling capacitance, the measured curve showed a strong dependence on the frequency. We analyzed the curve quantitatively based on the SPICE model of the strip and extracted the correct value for the coupling capacitance. Finally, a series of interstrip capacitances was measured between the DUT strip and its neighbor strips.

References

1. Y. Cai, Y. Li, L. Wen et al., Progress of single event effects and hardening technology of CMOS image sensors. Nucl. Tech. **43**, 010502 (2020). https://doi.org/10.11889/j.0253-3219.2020.hjs.43. 010502. (in Chinese)
2. H. Wang, C. Xu, C. Zhao et al., Chip position correction method for a multi-layer muon radiography detector. Nucl. Tech. **42**, 070403 (2019). https://doi.org/10.11889/j.0253-3219.2019.hjs.42. 070403. (in Chinese)
3. J. Sun, Q. Guo, Q. Zheng et al., Radiation response characteristics of an embeddable SOI radiation sensor. Nucl. Tech. **42**, 120501 (2019). https://doi.org/10.11889/j.0253-3219.2019.hjs.42. 120501. (in Chinese)
4. Z. Zhao, H. Xu, P. Gong et al., Management and query system for the beamline operation data based on archiver appliance at SSRF. Nucl. Tech. **41**, 030102 (2018). https://doi.org/10.11889/j.0253-3219.2018.hjs.41.030102. (in Chinese)
5. X. Xu, F. Teh, C. Lin et al., Characterization of CIAE developed double-sided silicon strip detector for charged particles. Nucl. Sci. Tech. **29**, 73 (2018). https://doi.org/10.1007/s41365-018-0406-0
6. D. Wang, C. Lin, L. Yang et al., Compact 16-channel integrated charge-sensitive preamplifier module for silicon strip detectors. Nucl. Sci. Tech. **31**, 48 (2020). https://doi.org/10.1007/s41365-020-00755-0
7. S. Wang, W. Chen, J. Guo et al., Design and testing of a miniature silicon strip detector. Nucl. Sci. Tech. **31**, 7 (2019). https://doi.org/10.1007/s41365-019-0714-z

8. J. Wei, A prototype silicon strip detector for space astronomy. Nucl. Tech. **41**, 120402 (2018). https://doi.org/10.11889/j.0253-3219.2018.hjs.41.120402. (in Chinese)

9. R. Turchetta, Spatial resolution of silicon microstrip detectors. Nucl. Instrum. Methods Phys. Res. Sect. A **335**, 44–58 (1993). https://doi.org/10.1016/0168-9002(93)90255-G

10. G. Barichello, A. Cervera-Villanueva, D.C. Daniels et al., Performance of long modules of silicon microstrip detectors. Nucl. Instrum. Methods Phys. Res. Sect. A **413**, 17–30 (1998). https://doi.org/10.1016/S0168-9002(98)00481-1

11. S. Ricciarini, PAMELA silicon tracking system: experience and operation. Nucl. Instrum. Methods Phys. Res. Sect. A **582**, 892–897 (2007). https://doi.org/10.1016/j.nima.2007.07.116

12. S. Straulino, O. Adriani, L. Bonechi et al., The PAMELA silicon tracker. Nucl. Instrum. Methods Phys. Res. Sect. A **530**, 168–172 (2004). https://doi.org/10.1016/j.nima.2004.05.067

13. G. Barbiellini, G. Fedel, F. Liello et al., The AGILE silicon tracker: testbeam results of the prototype silicon detector. Nucl. Instrum. Methods Phys. Res. Sect. A **490**, 146–158 (2002). https://doi.org/10.1016/S0168-9002(02)01062-8

14. E. Vallazza, G. Barbiellini, M. Basset, et al., The AGILE gamma ray satellite: the construction and performance of the silicon tracker. Paper presented at Nuclear Science Symposium Conference Record, IEEE, 2004. https://doi.org/10.1109/nssmic.2004.1462176

15. L. Latronico, G. Spandre, The GLAST large area telescope: design, construction, test and calibration. Nucl. Instrum. Methods Phys. Res. Sect. A **581**, 160–163 (2007). https://doi.org/10.1016/j.nima.2007.07.051

16. H. Tajima, GLAST tracker. Nucl. Instrum. Methods A **569**, 140–143 (2006). https://doi.org/10.1016/j.nima.2006.08.063

17. J. Alcaraz, B. Alpat, G. Ambrosi et al., The alpha magnetic spectrometer silicon tracker: performance results with protons and helium nuclei. Nucl. Instrum. Methods Phys. Res. Sect. A **593**, 376–398 (2008). https://doi.org/10.1016/j.nima.2008.05.015

18. P. Zuccon, The AMS silicon tracker: construction and performance. Nucl. Instrum. Methods Phys. Res. Sect. A **596**, 74–78 (2008). https://doi.org/10.1016/j.nima.2008.07.116

19. P. Azzarello, G. Ambrosi, R. Asfandiyarov et al., The DAMPE silicon–tungsten tracker. Nucl. Instrum. Methods Phys. Res. Sect. A **831**, 378–384 (2016). https://doi.org/10.1016/j.nima.2016.02.077

20. J. Chang, G. Ambrosi, Q. An et al., The DArk matter particle explorer mission. Astroparticle Phys. **95**, 6–24 (2017). https://doi.org/10.1016/j.astropartphys.2017.08.005

21. S. Ishikawa, S. Saito, H. Tajima et al., Fine-Pitch semiconductor detector for the FOXSI mission. IEEE Trans. Nucl. Sci. **58**, 2039–2046 (2011). https://doi.org/10.1109/tns.2011.2154342

22. S. Christe, L. Glesener, C. Buitrago-Casas et al., FOXSI-2: upgrades of the focusing optics X-ray solar imager for its second flight. J. Astronomical Instrum. **05**, 1640005 (2016). https://doi.org/10.1142/s2251171716400055

23. N. Bacchetta, D. Bisello, C. Calgarotto et al., A SPICE model for Si microstrip detectors and read-out electronics. IEEE Trans. Nucl. Sci. **43**, 1213–1219 (1996). https://doi.org/10.1109/23.506666

24. R. Qiao, W. Peng, X. Cui et al., A charge sharing study of silicon microstrip detectors with electrical characterization and SPICE simulation. Adv. Space Res. **64**, 2627–2633 (2019). https://doi.org/10.1016/j.asr.2019.07.005

25. T. Ohsugi, S. Yoshida, Y. Fukazawa et al., Design and properties of the GLAST flight silicon micro-strip sensors. Nucl. Instrum. Methods Phys. Res. Sect. A **541**, 29–39 (2005). https://doi.org/10.1016/j.nima.2005.01.035

26. Philipp Azzarello, Dissertation, University of De Geneve, 2004

27. N.L. Bruner, M.A. Frautschi, M.R. Hoeferkamp et al., Characterization procedures for double-sided silicon microstrip detectors. Nucl. Instrum. Methods Phys. Res. Sect. A **362**, 315–337 (1995). https://doi.org/10.1016/0168-9002(95)00280-4

28. W. Dabrowski, P. Gryboś, M. Idzik et al., Study of spatial resolution and efficiency of silicon strip detectors with different readout schemes. Nucl. Instrum. Methods Phys. Res. Sect. A **356**, 241–254 (1995). https://doi.org/10.1016/0168-9002(94)01398-5

29. Tektronix Inc., Model 4200A-SCS parameter analyzer reference manual (2019). https://www.tek.com/keithley-4200a-scs-parameter-analyzer-manual/model-4200a-scs-parameter-analyzer-reference-manual. Accessed 1 March 2020

30. Integrated Sensor Electronics AS (IDEAS) Inc., The product information of IDE1140. https://ideas.no/products/ide1140/. Accessed 20 June 2020